Journal of Magnetic Resonance Open 16–17 (2023) 100137

Contents lists available at ScienceDirect

Journal of Magnetic Resonance Open

journal homepage: www.sciencedirect.com/journal/journal-of-magnetic-resonance-open

Research Article

Magnetic resonance imaging and velocimetry of ethane

Maria Anikeeva [a,*], Maitreyi Sangal [b], Andrey N. Pravdivtsev [a], Maryia S. Pravdivtseva [a], Eva Peschke [a], Oliver Speck [b,c,d,e], Jan-Bernd Hövener [a]

[a] Section Biomedical Imaging, Molecular Imaging North Competence Center, Department Radiology and Neuroradiology, University Hospital Schleswig-Holstein (UKSH), Campus Kiel, Kiel University, Am Botanischen Garten 14, 24118, Kiel, Germany
[b] Department of Biomedical Magnetic Resonance, Otto-von-Guericke-University Magdeburg, Universitätsplatz 2, 39106, Magdeburg, Germany
[c] Center for Behavioral Brain Sciences, Magdeburg, Germany
[d] German Centre for Neurodegenerative Diseases, Magdeburg, Germany
[e] Leibniz Institute for Neurobiology, Magdeburg, Germany

ARTICLE INFO

Keywords:
Gas phase imaging
Gas relaxometry
Gas flow MRI
Spin echo imaging
Gradient echo imaging

ABSTRACT

This study investigates the experimental conditions required for magnetic resonance imaging (MRI) of thermally polarized hydrocarbon gas, focusing on ethane. The nuclear magnetic resonance (NMR) spectra and relaxation properties of ethane were analysed at different pressures in the range from 1.5 to 6 bar at 7 T using ^{1}H NMR spectroscopy. The spin-lattice relaxation time (T_1) and spin-spin relaxation time (T_2) were measured, and their dependence on the pressure was determined, showing that both relaxation times increase with pressure. Using the estimated relaxation times, we adjusted parameters for imaging of static ethane using rapid acquisition with relaxation enhancement (RARE) and fast low-angle shot (FLASH). The signal-to-noise ratio (SNR) of ethane images was evaluated and compared to the calculation for the given range of pressures. Then, we imaged flowing gas using a 2D velocity-encoded pulse sequence, which is usually used for liquid flow studies. The MRI-measured flow rates are compared to those pre-set with a pump, showing good agreement in the slow flow range. Overall, the results provide insights into the feasibility of ^{1}H MRI for imaging and flow measurements of thermally polarized ethane.

1. Introduction

Indispensable to a multitude of industrial sectors, processes involving gas flow reactions in reactors find widespread application in diverse fields such as food processing, pharmaceuticals, chemicals, and construction material production. Accurate measurements and simulations of these reactions in packed beds are essential to design more energy efficient reactors and for production of higher quality products. Parameters of interest include temporally and spatially resolved flow fields, temperature, pressure and chemical reactions (e.g. oxidation).

Not surprisingly, characterizing gas flow reactions in packed beds is an active field of research and has attracted much attention. Various methods are being investigated, but a gold standard for measuring all parameters has not emerged yet. Laser-based techniques like particle image velocimetry, offering outstanding velocity measurements [1], or laser doppler velocimetry [2] require optical access to closed reaction chambers or granular assemblies and can hardly be applied for reaction monitoring.

Magnetic resonance imaging (MRI) is an established method to image flow [3,4], temperature [5] and reactions [6] in liquids both qualitatively and quantitatively. MRI does not require optical access but relatively long scan times and cannot handle magnetic and conducting materials. A key challenge for gas-phase MRI is the low MRI signal of gases, which are much less dense compared to liquids, and the physical properties of the gases, such as relatively fast diffusion. One of the solutions is to use the hyperpolarization of nuclear spins that allows to boost the MR signal by several orders of magnitude, compensating for the low spin density of gases [7]. Inert noble gases, such as xenon-129 or helium-3, and hydrocarbons, e.g. propane, were previously hyperpolarized. For example, Koptyug et al. have successfully studied flow MRI of thermally polarized hydrocarbon gases under atmospheric pressures despite their low spin density [8,9] as well as of hyperpolarized gases with parahydrogen-induced polarization [10,11]. In another examples, hyperpolarized xenon-129 gas was used for imaging gas flow in [12,13] or for packed bed imaging [14]. To use this method, however, the gases need to be hyperpolarized first in specialized devices

* Corresponding author.
E-mail address: maria.anikeeva@rad.uni-kiel.de (M. Anikeeva).

https://doi.org/10.1016/j.jmro.2023.100137

Available online 13 October 2023

(the polarizer), which are still not widespread. Moreover, the costs of isotopically enriched xenon-129 considerably exceed the prices of hydrocarbons.

Returning to the application of thermally polarized gases for MR imaging, sulphur hexafluoride (SF_6) has been successfully used for studying the flow inside the packed beds [15] with resolution up to 0.35 × 0.35 mm [16]. While inert gas SF_6 has been examined in both laminar and turbulent flow regimes [17], hydrocarbon gases at thermal equilibrium (which requires no isotope labelling, rare gases and polarizers) show promise as they can be used for the investigation of chemical reactions in assemblies and packed beds. Focusing on imaging the gas flow field, we studied ethane (C_2H_6), which gives one strong CH_3 resonance, and present both static and velocity-resolved images. Aside from the molecule, the actual imaging methods require some attention, too, as most methods were developed for liquids whose properties are different to gases. Most of the approaches for gas phase MRI studies were based on the assumption of short T_2-relaxation times, and consequently gas images were acquired with the sequences designed for spins with short T_2, e.g. single-point ramped imaging with T_1 enhancement (SPRITE) [18] or ultrashort echo time (UTE) [19]. Nonetheless, gas flow measurements have also been successfully accomplished using pulsed field gradient sequences [9], which are traditionally employed in MR experiments for liquid flow. Ulpts et al., using magnetic resonance spectroscopy imaging (MRSI), investigated ethylene hydrogenation at ambient pressures [20]. The authors also highlighted the potential enhancement of the signal-to-noise ratio (SNR) of gases by utilizing improved imaging parameters, which can be determined based on known T_1 and T_2 values, as well as data on gas flow velocities during catalytic reactions. In this context, a recent study by Duchowny et al. [21] focused on investigating the chemical shifts and relaxation times of methane and its mixtures with ethane across a large pressure range of up to 200 bar reaching an SNR of 17,400 for 200 bar pressurized gas. Considering these impressive results from the spectroscopy of hydrocarbons, we aim to study the optimal experimental conditions and MRI parameters. We investigate the conditions for gas imaging and flow experiments with ethane – necessary steps for studying packed beds or gas flow reactions. We determined the essential MRI parameters (T_1 and T_2) at different pressures and demonstrated both static and flow-resolved MRI under 7 T with optimized parameters with and without a 3D printed structure.

2. Methods

2.1. Gas-phase MRI setup

To investigate the nuclear magnetic resonance (NMR) characteristics of ethane gas, including the T_1 and T_2 relaxation times, we employed a 26 mm borosilicate flask (model P170002, Synthware, Hong Kong) with an inner diameter (ID) of 20 mm, a length of 80 mm, and a volume of 75 mL. This flask is designed to withstand pressures of up to 6 bar. The flask was filled with ethane (C_2H_6) of 3.5 grade (99.95% purity, Linde plc, Dublin). MR images of ethane were obtained by filling an empty flask solely with ethane or by inserting an additional 3D-printed structure (Fig. 1(a)). The structure consisted of small spheres with a diameter of approximately 9 mm, printed in a body-centred cubic (bcc) packing configuration with a length of 70 mm; the spaces between the spheres were approximately 1 mm. The spheres were printed from urethane dimethacrylate ("clear resin", Formlabs, Somerville) on a stereolithography (SLA) printer (Form 3, Formlabs). The resulting assembly of spheres printed from clear resin were smooth without visible structural defects.

Ethane flow was measured in a different configuration, wherein it was directed through a 6 mm polyurethane tubing (Shan Hua Plastic

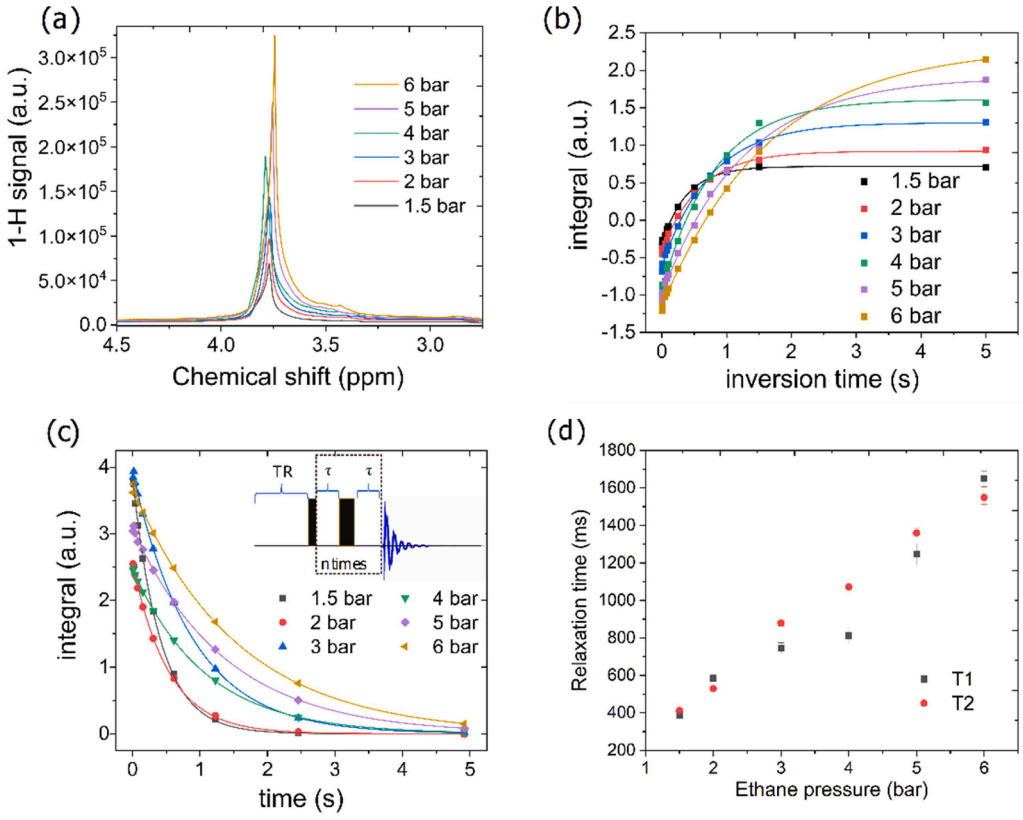

Fig. 1. Three gas setups utilized in this study. An empty flask (a) was filled with ethane of various pressures to analyze the relaxation behavior of the gas. MR imaging of static ethane was done in two configurations: (a) an empty flask and (b) a flask filled with 3D printed structures. Additionally, a separate gas setup (c) was designed and employed specifically for gas flow measurements. The majority of the components comprising this system were positioned outside the MRI room, resulting in an overall length of the polyurethane tube of approximately 10 m.

Industrial, Taiwan) with a 4 mm inner diameter. This tubing formed a closed cycle that passed through the bore of the MRI machine, as depicted in Fig. 1(b). The gas flow was generated using a small gas pump, which was able to create a flow rate up to 192 L/h. The motor speed and consequently the flow rate was controlled by a power source unit (NGL 202, Rohde & Schwarz, Munich). The exact flow rate value was monitored using a variable area flow meter with a float (1AF-M1–01M-1–0, Swagelok, Solon). We note that the flow meter was pre-calibrated for air at 20 °C and 1 bar. Therefore, ethane flow was calculated from the value indicated by the flow meter (f_{ethane}=f_{air}·F) using a calibration factor, F:

$$F = \sqrt{\frac{\rho_{air}}{\rho_{gas}}}\cdot\sqrt{\frac{P_{gas}}{P_{air}}}\cdot\sqrt{\frac{T_{air}}{T_{gas}}} \quad (1)$$

Here ρ indicates density, P – pressure and T – temperature of air or the gas under investigation, i.e. ethane in our case.

Gas pressure on the outlet side of the MRI machine was monitored using a pressure gauge (316 SS EN 837–1 with maximum measuring pressure of 10 bar, Swagelok). During the measurement, an increase in pressure of approximately 0.25 bar with respect to the nominal value set by the pressure reducer on the gas bottle (3 bar) was observed. Although all the tubes forming the closed cycle had a fixed inner diameter of 4 mm, this pressure increase originates from the smaller inlet and outlet diameter of the pump of ~ 2 mm. Prior to the experiment, the gas line was flushed with ethane using a one-way quarter-turn valve as an exhaust mechanism. All connection parts, adapters, and valves utilized in the setup were constructed from stainless steel components (Swagelok).

2.2. Magnetic resonance measurements

2.2.1. Magnetic resonance hardware

All magnetic resonance experiments in this work were performed on a 7 T pre-clinical MRI (BioSpec, Bruker, Billerica), equipped with a 3D gradient system with gradient strength of 600 mT/m and maximum slew rate of 4570 T/m/s. For the measurements, we used a ^{1}H transmit-receive quadrature volume resonator (86 mm inner diameter, Bruker). This geometry allowed for the imaging of the entire gas flask. Note that the B_1 field is almost homogeneous, i.e. deviates by ± 5% from the average B_1 value in the middle of the coil. The overall length of this homogeneous part is approximately 36.6 mm, and the B_1 field goes down by 30% from the maximum in the middle to the sides of the flask (see details in Supplementary material, Fig. S1).

2.2.2. Magnetic resonance spectroscopy and relaxometry

The free induction decay (FID) of ethane's protons was measured after a single 90° radiofrequency (RF) pulse (quadrature excitation from two r.f. coil channels, 90° rectangular pulse was calibrated to 200 W and 70.7 μs, acquisition time of 0.517 s, spectral width of 30 ppm, number of averages N_{avs}=1). Before the signal acquisition, the system was calibrated on the flask filled with ethane to 6 bar: the resonator was tuned to ^{1}H frequency using variable capacitors (tune and match), then basic (central) frequency, reference power and receiver gain were automatically adjusted, as well as B_1 field was automatically calibrated (*ParaVision 360 V 2.0,* Bruker). Additional manual shimming was performed by changing the linear harmonics (X, Y, Z) while monitoring the spectrum in situ. The peak position and full width at half maximum (FWHM) of the ethane signal were derived by fitting a Lorentzian function for the dominating peak (*Top Spin* 4.1.1, Bruker). Only phase and baseline correction without line broadening or zero-filling was applied during post processing. Before the analysis, the background signal of a flask filled with air was subtracted from each spectrum. The signal-to-noise (SNR) values were calculated as the ratio between the ethane peak height divided by the root-mean-square of a noise area in the spectrum.

Additionally, an ethane spectrum inside a gas-tight thick-wall 5 mm NMR tube (513–7PVH-7, Life Science Wilmad, Vineland) was measured on a 9.4 T NMR spectrometer (WB400, Avance NEO, 5 mm BBFO probe). In this experiment, we first performed the shimming on deuterated methanol CD_3OD (methanol-d4), and then added pressurized ethane gas of 3 bar to the same tube. After adding the gas, the tube was shaken for several seconds, and shimming was repeated. Finally, the ^{1}H-spectrum of the gas and liquid mixture was acquired using a 90° rectangular pulse (linear excitation with 24.9 W and 10 μs, spectral width of 99 ppm, four averages, recycle delay time of 5 s and acquisition time of 1 s).

The longitudinal relaxation time, T_1, was measured at different pressures via an inversion recovery (*IR*) sequence (180° pulse - inversion time, TI, – 90° pulse, TI = 0.001 s, 0.005 s, 0.01 s, 0.05 s, 0.075 s, 0.1 s, 0.25 s, 0.5 s, 0.75 s, 1 s, 1.5 s, 5 s, N_{avs} = 4, recycle delay time of 5 s, linear (no quadrature) excitation using one channel, 90° block pulse calibrated to 200 W and 100 μs, 180° pulse was set to 200 μs).

The changes in longitudinal magnetization M_z(t) monitored in *IR* experiment is usually modelled by an exponential decay function:

$$M_z(t) = M_z^0\cdot\left(1 - B\cdot e^{-\frac{TI}{T_1}}\right) \quad (2)$$

where M_z^0 is an equilibrium magnetization and parameter B represents the rotation of the magnetization in the *IR* experiment, where B = 2 corresponds to the ideal inversion induced by the first 180° pulse.

To derive the transverse relaxation time, T_2, we used a variant of the Carr-Purcell-Meiboom-Gill (*CPMG*) sequence: $90°_X$-$(\tau - 180°_Y - \tau)^{n180}$-acquisition [22] (inset in Fig. 2(c)) [23,24] with n_{180} spin echo elements between 12 and 6144, τ = 300 μs and N_{avs}=4. With the refocusing pulses of 200 μs (linear excitation from one channel of the r.f. coil), effective echo times (i.e. the time between excitation pulse centre and beginning of signal acquisition) were between $12\cdot(600\,\mu s + 200\mu s) = 0.0096\ s$ and $6144\cdot(600\,\mu s + 200\mu s) = 4.9\ s$.

To estimate the transverse relaxation time, T_2, we used a mono-exponential model for net magnetization of the CPMG echo train with two-parameters, M_{xy}(0) and T_2:

$$M_{xy}(t) = M_{xy}(0)\cdot e^{-\frac{n_{180}(2\cdot\tau + p_{180})}{T_2}} \quad (3)$$

where M_{xy}(0) is the transverse magnetization directly after the application of 90° pulse, n_{180} is the number of refocusing pulses and p_{180} is the duration of the 180° pulse.

Thus, relaxation times T_1 and T_2 and standard errors were derived by fitting Eqs. (2) and (3) to corresponding experimental data using linear error propagation[1] (*Origin Pro*).

The dephasing relaxation time T_2* was recalculated from FWHM of the signal spectra as:

$$T_2^* = \frac{1}{\pi\cdot FWHM} \quad (4)$$

The diffusion of the gas during the experiment can influence the observed signal. So, in the CPMG experiment, during the echo interval, (2·τ), the average displacement of the gas molecules due to diffusion can be calculated as [25]:

$$\Delta r = \sqrt{6\cdot D\cdot(2\cdot\tau)} \quad (5)$$

2.2.3. Magnetic resonance imaging

Ethane imaging was performed with a fast-low angle shot (FLASH) gradient echo (GRE)-based sequence, and rapid acquisition with relaxation enhancement (RARE) turbo spin echo (SE) pulse sequence. Both were available in *ParaVision 360 V 2.0,* Bruker. The scans using RARE and FLASH were repeated five times for each pressure to check for the reproducibility of the measurement. We note, that these repeated

[1] The standard error was calculated as a square root of sum of partial derivatives for each variable and the derivatives of their covariances.

measurements were done within one day to maintain the same MRI machine adjustments.

We used the following parameters for FLASH: constant TR = 200 ms, field of view (FOV) = 58 × 58 mm, image matrix size of 64×64 pixels, slice thickness of 80 mm, bandwidth (BW) of 5 kHz, N_{avs} = 8, with centric phase encoding and TE = 7.562 ms; this TE was chosen as the shortest possible. The excitation angle was adjusted for each pressure in respect to the measured relaxation time T_1. The total duration of the FLASH sequence is given by:

$$T_{tot}\ (\mathrm{FLASH}) = N_{avs} \cdot TR \cdot N_{ph} \tag{6}$$

where N_{ph} is the number of phase-encoded lines in k-space, here e.g., we used 64. In general, the signal of FLASH [26] depends on the aforementioned parameters as follows:

$$S^{FLASH} \sim \frac{\sin\alpha \cdot \left(1 - e^{-\frac{TR}{T_1}}\right) \cdot e^{-\frac{TE}{T_{2^*}}}}{\left(1 - e^{-\frac{TR}{T_1}} \cdot \cos\alpha\right)} \tag{7}$$

For the selected *TR* and fixed total duration of experiment, the SNR achieves its maximum when the so-called Ernst angle is used:

$$\alpha_E = \arccos\left(e^{-\frac{TR}{T_1}}\right) \tag{8}$$

For the RARE imaging, we kept the same geometry as for FLASH and used the following acquisition parameters: FOV = 58 × 58 mm, slice thickness of 80 mm, image matrix size of 64×64 pixels with centric phase encoding, BW = 5 kHz, but changed the TE = 15.36 ms and set RARE factor (number of acquired echoes per excitation) N_{RARE}= 2. TR and N_{avs} were selected according to the relaxation time of ethane, which is a pressure-dependent parameter.

For RARE, the total acquisition time can be calculated similar to Eq (6) but including the acceleration factor N_{RARE}:

$$T_{tot}\ (\mathrm{RARE}) = \frac{N_{avs} \cdot TR \cdot N_{ph}}{N_{RARE}} \tag{9}$$

The signal of RARE [27] imaging depends on the aforementioned parameters as follows:

$$S^{\mathrm{RARE}} \sim e^{-\frac{TE}{T_2}} \cdot \left(1 - 2 \cdot e^{-\frac{TR - \frac{TE}{2}}{T_1}} + e^{-\frac{TR}{T_1}}\right) \tag{10}$$

A 3D FLASH imaging of the flask with ethane gas and the 3D printed bcc structure was acquired using following sequence parameters: TE = 3.087 ms, TR = 100 ms, N_{avs} = 36, BW = 50 kHz, excitation angle α = 28°, FOV = 50 × 50 × 40 mm, resolution = 0.521 × 0.521 × 4 mm and image matrix size = 96 × 96 × 10 pixels.

2.2.4. Estimation of the signal-to-noise ratio

In general, the SNR of an MRI image is affected by many factors: (1) magnetization of the media contributing to the signal (this term includes the spin density $N(^1\mathrm{H})$, the gyromagnetic ratio of the nuclei, temperature, and the main magnetic field B_0); (2) frequency of the nuclei; (3) r.f. coil's quality factor; (4) volume of the object; (5) number of averages, N_{avs}; (6) bandwidth (BW); (7) filling factor of the coil with an object; and (8) the sequence used for imaging (here, FLASH and RARE) [28,29]. In the current work, we kept most of the parameters the same: magnetic field, nuclei (protons), quality and filling factor of the coil (quadrature volume coil with the same flask filled with the gas), bandwidth, voxel size (Δx, Δy) and slice thickness (Δz). Other parameters can be optimized for FLASH (Eq. (8)) or RARE (Eq (11)) sequences or are functions of the gas pressure ($N(^1H)$). As a result, in our case the difference between the pulse sequences and pressures can be represented as:

$$SNR^{\mathrm{FLASH\ or\ RARE}} \sim N(^1\mathrm{H}) \cdot \sqrt{\frac{N_{avs}}{BW}} \cdot S^{\mathrm{FLASH\ or\ RARE}} \tag{11}$$

Where the spin density, $N(^1\mathrm{H})$, is calculated as:

$$N(^1\mathrm{H}) = \frac{N_a \cdot n \cdot \rho}{M} \tag{12}$$

Here, N_a is Avogadro's number ($6.02 \cdot 10^{23}$ mol^{-1}), n is the number of nuclear spins in a molecule (6 for ethane), M is the molar mass (0.03007 kg/mole for ethane), and ρ the gas density, which is a pressure dependent parameter and can be calculated as:

$$\rho = \frac{P \cdot M}{R \cdot T} \tag{13}$$

where T is the room temperature (293 K), P is the gas pressure (from 1.5 to 6 bar in our experiments), R is the gas constant (0.0821 L·bar/mole·K).

The SNR in all experimental 2D and 3D MR images was calculated as the mean signal from the sample divided by the standard deviation of the noise signal outside the sample (see Figs. 3 and 5 in Results Sections 3.2 and 3.3 correspondingly). In the case of the 2D FLASH and RARE imaging, the SNRs were calculated as mean values from the series of five images done for each pressure; STDs from these SNR values were used as errors (see further in Tables 2, 3 and Fig. 4(a), (b) in Section 3.2).

2.2.5. Magnetic resonance velocimetry

Ethane flow was studied using a flow-compensated gradient echo sequence (FLOWMAP, *Para Vision 360 V 2.0,* Bruker). This sequence is a modification of FLASH used for gas imaging. It incorporates a flow compensation technique to eliminate undesired phase shifts in the signal arising from fluid movement. To assess the velocities, bipolar gradient pulses are introduced during the encoding period, generating phase contrast changes, which depend on the flow rate. In this experiment, we studied ethane flow at different velocities inside a 4 mm inner diameter tube at 2 bar (Fig. 1(b)). Velocity was measured in one direction perpendicular to the selected slice, corresponding to the longitudinal velocity component. The velocity encoding parameter (*venc*) that should be selected to account for the highest expected velocity from the measurement was changed for different flows set by the pump. The pump produced a flow ranging from 5 L/h to 50 L/h, which corresponded to flow rates of ethane from 7.2 L/h to 71.6 L/h calculated by Eq (1). Thus, venc was increased in a range from 75 cm/s up to 300 cm/s, adapting to the motor speed of the pump. The FLOWMAP scans were acquired using the following parameters: 0.375 × 0.375 mm resolution, TE = 2.2 ms, TR = 50 ms, α = 25°, N_{avs} = 36, FOV = 30 × 30 mm, slice thickness 40 mm, axial slice orientation and total duration of 5 min. For velocity evaluation, a FLOWMAP image of the static gas (the pump was switched off) with the same parameters was acquired and used for background signal correction of the velocity encoded images. The measured velocity magnitude in the imaging plane was linearly interpolated, increasing the total number of points by 2. These interpolated values were visualized voxel-wise using a colour-coded representation (MATLAB R2023a, MathWorks, Natick, MA, USA). The flow rate, f, from the magnetic resonance velocimetry (MRV) images was calculated as a product of the mean velocity values of the gas, v, inside the tube and the cross-section of the area:

$$f = v \cdot S_{\mathrm{area}} \tag{14}$$

Additionally, we calculated Reynolds numbers for the gas flow:

$$Re = \frac{v \cdot d_t \cdot \rho}{\eta} \tag{15}$$

where d_t is the inner diameter of the tube and η_{dyn} is the dynamic viscosity, which was calculated according to the formula for the ideal gas:

$$\eta_{dyn} = \sqrt{\frac{4 \cdot k_B \cdot T \cdot m}{9 \cdot \pi^3 \cdot d_{C2H6}^4}} \tag{16}$$

Where m is the mass ($4.99 \cdot 10^{-26}$ kg) of the ethane molecule.

3. Results

3.1. Nuclear magnetic resonance measurements of ethane

First, non-localized ^{1}H NMR spectra of ethane were measured at pressures from 1.5 bar to 6 bar at 7 T MRI system using a 90° RF pulse. A single scan yielded an ethane peak at around 3.8 ppm with an SNR of 1500–6700 (Table 1, Fig. 2(a)). An elevation of the signal on the right side of the peak at about 3.5 ppm was attributed to imperfect shimming. This was confirmed by high resolution NMR spectroscopy at 400 MHz: the spectrum of dissolved ethane in methanol-d4 had a FWHM of 1.5 Hz and did not feature any impurities in the gas (not shown here).

The spin-lattice relaxation time increases steadily from T_1 (1.5 bar) = 386 ms to T_1 (6 bar) = 1649 ms. The mean value of the inversion parameter, B (Eq (2)), for different pressures was 1.49 ± 0.05, indicating incomplete inversion of spins. The results of the CPMG experiment were similar: T_2 increased with the pressure from T_2 (1.5 bar) = 409 ms to T_2 (6 bar) = 1550 ms. We note that for some pressures (1.5, 3, 4 and 5 bar), spin-spin relaxation time was measured slightly higher than spin-lattice relaxation time.

At the same time, dephasing time, T_2*, calculated from the FWHM of the spectra according to Eq (4), did not change considerably between the different pressure settings with a mean value of 15.8 ms. Both relaxation times increased monotonously with pressure.

3.2. Ethane 2D imaging. comparison to calculation

The 75-mL flask filled with ethane at different pressures was imaged on the 7 T MRI. As described in Section 2.2.3, two imaging sequences were tested: FLASH (Fig. 3(a)-(c)) and RARE (Fig. 3(d)-(f)). The imaging time was kept at 100 s for each scan. We note that some of the imaging parameters were adjusted with respect to the relaxation times measured above, i.e. flip angle in FLASH sequence, repetition time and number of averages in RARE.

Then, using Eqs. (6)–(13) we estimated SNR values for different pressures. The most essential parameters contributing to the SNR in FLASH and RARE are assembled in Tables 2 and 3 correspondingly. Although the calculation of the SNR factor (Eq (11)) does not give a quantitative result, but gives a trend for variation of pressure or other parameters of MRI sequences.

According to the calculation, the SNRs of the RARE sequence were, in general, higher than the values expected for the FLASH sequence (black dots in Fig. 4(b) and black squares in Figure (a) correspondingly). The rising of pressure led to higher calculated SNR values; however, starting from 4 bar, the SNR reached a plateau for the FLASH calculation or slowed down to rise for the RARE. Experimentally, the SNR of the RARE images increased steadily for ethane at 5 and 6 bar (blue dots in (b)). As for the FLASH images overall, the SNR values varied in a smaller range between 195 and 277 as compared to the RARE values that changed between 164 and 430. Moreover, unexpectedly, the SNR of the ethane FLASH image for ethane at 5 bar dropped from 287 to 204 and then rose again at 6 bar to 277.

Table 1
^{1}H spectroscopy results of ethane: chemical shift, FWHM, T_2* (Eq (4)), SNR of single acquisition, T_1 and T_2 relaxation times with their standard errors from the fitting (Eq (2)-Eq (3)). T_1 and T_2 are plotted in Fig. 2(d). The fitting accuracy was monitored by checking the R-square parameter, which was 0.99834 on average for T_1 and 0.95947 for T_2.

Pressure [bar]	Chemical shift [ppm]	FWHM [Hz]	T2* [ms]	SNR	T_1 [ms]	T_2 [ms]
1.5	3.769	19.9	16.0	1577	386 ± 16	409 ± 13
2	3.770	21.2	15.0	1888	583 ± 21	526 ± 15
3	3.769	20.6	15.5	3285	747 ± 28	879 ± 23
4	3.783	18.0	17.7	3979	812 ± 44	1067 ± 31
5	3.758	18.9	16.8	4571	1248 ± 57	1362 ± 47
6	3.748	20.5	15.5	5719	1649 ± 43	1550 ± 68

3.3. 3D ethane imaging

To assess sensitivity of MRI to image reaction chambers, we acquired 3D MR images of the flask filled with 4 bar ethane using a 3D FLASH sequence. Imaging parameters were slightly modified to find a balance between the image resolution, echo time and total scan time. Here, similar values of SNR of approximately 80 for the flask without and with a bcc structure were found. We note, that the SNR was lower than the SNR measured in the 2D experiment due to the thinner slice used in imaging: slice thickness in 3D FLASH was 4 mm while in 2D FLASH - 80 mm.

3.4. Magnetic resonance velocimetry of ethane

After optimizing the imaging of ethane on static gas, we proceed with measuring MRI of a gas flow. For this, a FLOWMAP sequence was used and velocity-encoded 2D MR images were acquired within 5 min each. The accuracy of gas flow measurements using the MRI was estimated by comparing the experimental data to the flow rate set by the pump. In consideration of safety precautions, the pump-driven circuit was employed in this study at 2 bar pressurized ethane. The gas flow inside a 4 mm-diameter tube was varied from 7.2 L/h to 71.6 L/h with steps of 7.2 L/h. The *venc* (velocity encoding parameter) was incremented accordingly.

Overall, flow rates measured by MRI showed a good agreement with the values measured with the flow meter in the slow flow range, approximately up to 35.8 L/h. At the same time, the highest experimental values corresponding to the pump flows of 64.5 L/h to 71.6 L/h underestimate these pre-set values by 30%. With the Reynolds numbers below 2000, a laminar flow inside the tube is expected for all flow rates. Indeed, the observed parabolic profile characteristic for laminar flow, with the velocity maximum in the centre of the tube that decays towards the edges, was observed (Fig. 5(f)–(h)).

4. Discussion

In this work, we investigated the experimental conditions required to perform MR imaging of thermally polarized hydrocarbon gas, specifically ethane. Ethane, a symmetrical molecule, contains six hydrogen atoms whose NMR spectrum features a single narrow line. Despite the low spin density of the gas phase, one 90° pulse with no further averaging was enough to gain an SNR of around 1500 for 75 mL of ethane at 1.5 bar (Table 1).

Our experimental T_1 and T_2 values measured at 7 T were comparable to each other and exceeded 1 s at pressures above 5 bar. Indeed, the theory of molecular motion [30] predicts that in gases *inter*molecular interactions can be considered negligible and only *intra*molecular and spin-rotation interactions should be considered (for liquids or solids all the components should be taken into account). For rapidly tumbling gas molecules, the intramolecular and spin-rotation correlation times are extremely short, in the range of *ps* [31]. In such extreme narrowing regime, the T_1 and T_2 not only increase but tend to be equal [30].

Then, the inversion parameter, *B*, from Eq (2) was ~ 1.5, indicating an incomplete longitudinal magnetization inversion. We explain such deviation by the inhomogeneity of our r.f. coil, especially on its edges, where the B_1 dropped by more than 30% (see Supplementary material, Fig. S1). Notably, the homogeneous area of the coil was only ~ 40 mm – half of the total length of the flask (80 mm). One of the solutions would be to use a shorter flask or restrict the gas in the 40 mm homogeneous

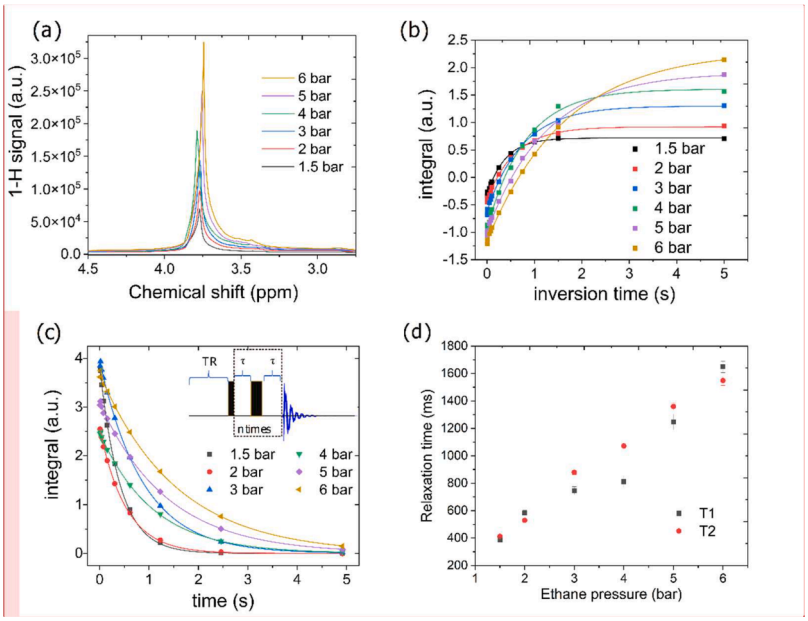

Fig. 2. ^{1}H NMR spectra and relaxation of ethane at 7 T and various pressures. (a) ^{1}H NMR spectra were acquired after 90° excitation with the same receiver gain (*rg* = 10.48) and without averaging. The integrals of the ^{1}H ethane signal in (b) IR (dots) and (c) CPMG (dots) experiments were fitted by the mono-exponential functions (Eq (2)) and (Eq (3)) to determine the T_1 (b, solid curve) and T_2 (c, solid curve). We note that values of the integrals were divided by 10^8. (d) Summary of the T_1 and T_2 data depending on ethane pressure (also listed in Table 1). The inset in (c) shows the scheme of the CPMG sequence used in the current work.

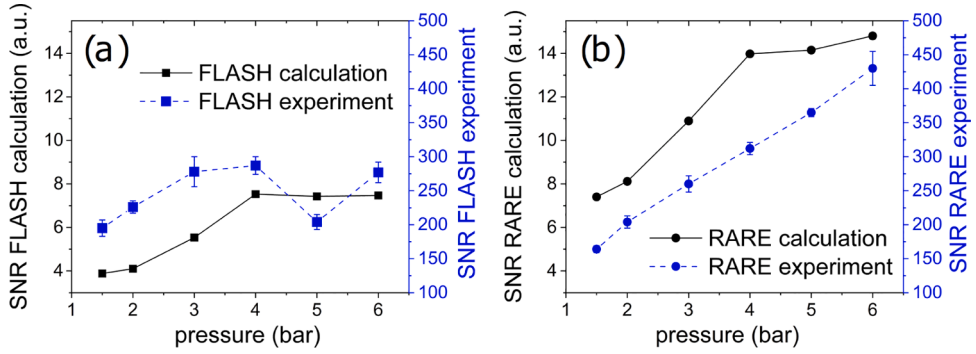

Fig. 3. ^{1}H FLASH (a)–(c) and RARE (d)–(f) MR images show axial projections of the flask filled with ethane at 1.5 (a, d), 4 (b, e) and 6 bar (c, f). The images of the first scans (out of five images done for each pressure) are presented. Phase encoding was done in *y* and read in - *x* directions, in-plane resolution was 0.906 × 0.906 mm with the slice thickness of 80 mm giving the voxel size of 65.7 mm^3; all other imaging parameters are listed in Section 2.2.3 Magnetic resonance Imaging. For SNR calculation, the mean values of the signals inside the flask (marked with orange circles in (a), (d)) were divided by the root-mean-square of a noise signal outside of the flask (marked with orange square boxes in (a), (d)) was calculated. We note that for the sake of comparison, the same contrast level was set in all images as shown on the grayscale.

Table 2
Estimated SNR of ethane for the FLASH sequence as a function of pressure in a fixed scan time of 100 s. In the last column, mean SNR values measured from the repeated experimental FLASH images together with the STD from the image series are listed (Fig. 3(a)-(c)). TR=200 ms, TE= 1.892 ms, N_{ph}=64, BW = 5 kHz, and N_{avs} = 8 (Eq (6)) – the same as for imaging - were used. Ernst angle was calculated according to Eq (8).

Pressure [bar]	Ethane density [g/L]	Spin density [10^{23} L^{-1}]	Ernst angle α [°]	SNR factor FLASH [10^{19} a.u.]	Experimental SNR (FLASH)
1.5	1.851	2.22	53.4	3.88	195 ± 12
2	2.467	2.96	44.8	4.10	226 ± 9
3	3.701	4.45	40.1	5.54	278 ± 22
4	4.935	5.93	38.6	7.53	287 ± 13
5	6.168	7.41	31.6	7.43	204 ± 11
6	7.402	8.89	27.7	7.47	277 ± 15

Table 3
Estimated SNR of ethane for the RARE sequence as a function of pressure in a fixed scan time of 100 s. In the last column, mean SNRs measured from the experimental RARE images and the corresponding STDs calculated from the repeated measurements are listed (Fig. 3(d)-(f)). In the calculation TR=2·T_1, TE=15.36 ms, N_{ph} = 64, number of echoes N_{RARE} = 2, BW = 5 kHz were used, the same as for imaging. Values for the relaxation times T_1 were taken from Table 1.

Pressure [bar]	TR [s]	Experimental N_{avs}	SNR factor RARE [10^{19} a.u.]	Experimental SNR (RARE)
1.5	0.772	4	7.4	164 ± 5
2	1.166	3	8.1	204 ± 9
3	1.494	2	10.9	260 ± 12
4	1.624	2	14.0	312 ± 9
5	2.496	1	14.2	365 ± 6
6	3.298	1	14.8	430 ± 25

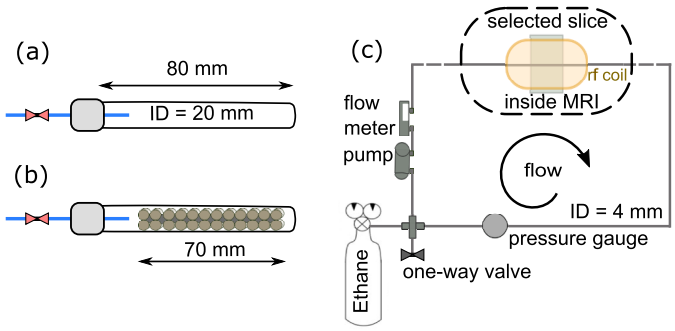

Fig. 4. Calculated SNR ratio for FLASH (black squares in (a)) and RARE (black circles in (b)) as a function of pressure and the corresponding mean SNR values derived from the repeated five times experimental FLASH (blue squares in (a)) and RARE (blue circles in (b)) images shown in Fig. 3 for a total scan time = 100 s. Note a similar trend for calculated SNRs for FLASH and RARE, where experimental values especially for FLASH imaging deviate from the calculation. We note, that the absolute values for calculated SNR were divided by 10^{19}. The scales for calculated (3 – 15.5 a.u.) and measured (100 - 500) SNRs were set the same between RARE and FLASH for the sake of comparison. Error bars around the experimental values indicate the STDs calculated from the RARE and FLASH image series.

area. Nevertheless, the estimation of the T_1 itself would not be affected by the inversion of less than 180° as can be seen from Eq. (2). Also, to account for the long T_1 at 5 and 6 bar, we have repeated the measurement with a longer delay time of 10 s, which resulted in very similar values to the ones listed in Table 1.

Previous works have already investigated hydrocarbon gases in some detail, providing values for relaxation times [8,21,32,33]. T_1 and T_2 values for acetylene (205 ms and 150 ms) and propane (995 ms and 586 ms) were reported for ambient pressure [8]. For methane, T_1 of 200 bar was measured at 4.5 s and T_2 – of 2.5 s [21]. Though, only a few works on the ethane relaxation times could be found in literature: King et al. reported the T_1 relaxation time of 1.25 s for approximately 3.5 bar, 2.25 s – for 6.9 bar and around 10 s – for 34 bar [34]. At the same time, Zhang et al. also measured the longitudinal relaxation time at approximately 10 s for approximately 100 bar pressure gas[2] [32]. Our relaxation data from pressure range between 1.5 bar and 6 bar are, thus, consistent with prior results and as shown before, both T_1 and T_2 increased together with the pressure [21]. A relation between the relaxation times of diluted gases (i.e. where the collisions between molecules can be considered absent) and gas pressures was first described by Bloom et al. for methane [35]. Theoretically and experimentally, it was shown that for higher pressures, the correlation time monotonously decreased and, as a result, the relaxation times increased.

Moreover, one can expect that the relaxation times of hydrocarbon gases is independent of the magnetic field strength (Eq. (17)). Spin-lattice relaxation rates can be described using normalized spectral density J(ω), which is defined as:

$$J(\omega) = \frac{\tau_c}{1 + \omega^2 \cdot \tau_c^2} \tag{17}$$

where ω is a Larmor frequency ($\omega = B_0 * \gamma$) and τ_c – correlation time. As mentioned, in the extreme narrowing regime for diluted gases: $\omega * \tau \sim 10^{-6} << 1$. Thus, the only term containing magnetic field strength involved in the relaxation rate can be neglected. For a full theoretical description of the gas relaxation mechanisms, we refer to the equations from Ref. [35]. Indeed, reviewing the sparse experimental data on the

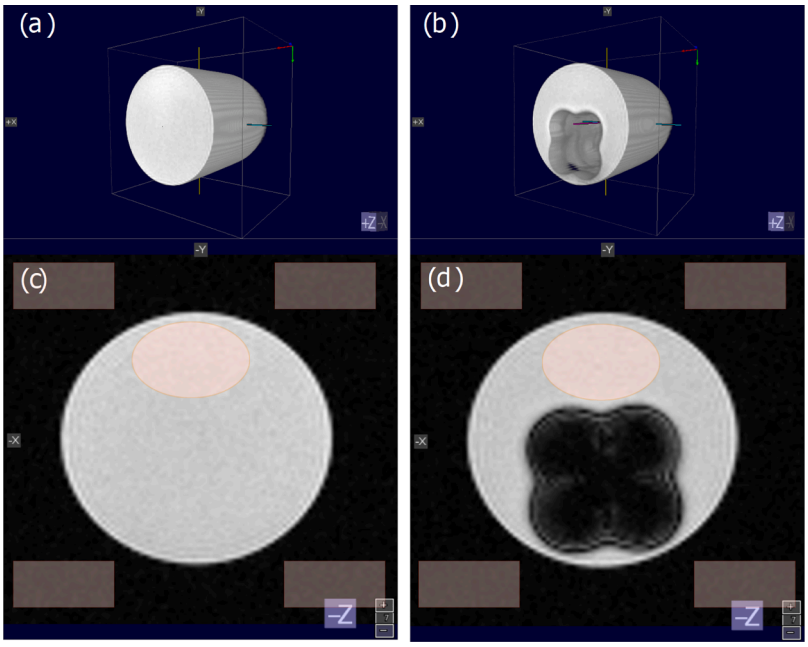

Fig. 5. ^{1}H 3D FLASH image of 4 bar ethane without (a) and with 3D printed structure (b) acquired in 60 min. In the lower row, a single selected slice (4 mm thick) is presented. Imaging parameters were slightly different from the 2D experiment: TE = 3.087 ms, TR = 100 ms, N_{avs} = 36, α = 28°, FOV = 50 x 50 x[ADM1] 40 mm^3, resolution = 0.521 x 0.521 x 4 mm^3 and image matrix size = 96 x 96 x 10 pixels. For SNR calculation, the signal from ethane and STD outside the flask was measured in the 7th slice (c), (d) as marked by orange areas in (d). Blurring in the area of the 3D-printed structure inside the flask in (d) may be explained by different rows of spheres arranged in the bcc structure which are coinciding within one slice (4 mm) selected for 2D imaging. No significant degradation of image quality was found when the printed structure was inserted. [ADM1]Reviewer 1, 16)

[2] The exact pressure value was not indicated by the authors, we re-calculated it from the diffusion coefficients provided in their work.

Table 4
Summary of the results studied in the MRV experiment: velocities measured by MRI can be compared to the velocity setting calculated from the flow rates indicated by the flow meter (set flow). Interestingly, increasing the flows by the flow meter leads to a lower measuring accuracy of the MRI, i.e. measured-to-set flow ratio. Reynolds numbers were calculated from the measured velocities using Eq (17). We note that ethane flows set by the pump (second column) were re-calculated from the nominal values shown on the flow meter calibrated initially for air (first column) using a calibration factor F=1.433 (Eq (1)).

Flow metre setting (air) [L/h]	Ethane flow setting [L/h]	venc [cm/s]	Measured mean MRI velocity [cm/s]	Measured area [cm^2]	Measured MRI flow [L/h]	Measured-to-set flow ratio	Reynold's number
0	0	75	−1.3		–	–	–
5	7.2	75	27.2	0.0956	9.4	1.3	312
10	14.3	100	41.7	0.0984	14.8	1.0	477
15	21.5	100	54.7	0.097	19.1	0.9	626
20	28.7	150	71.4	0.0956	24.6	0.9	817
25	35.8	175	83.3	0.0942	28.2	0.8	953
30	43.0	200	98.4	0.0956	33.9	0.8	1127
35	50.1	250	111.1	0.0956	38.2	0.8	1272
40	57.3	250	123.1	0.0984	43.6	0.8	1410
45	64.5	300	136.8	0.0956	47.1	0.7	1566
50	71.6	300	148.4	0.097	51.8	0.7	1699

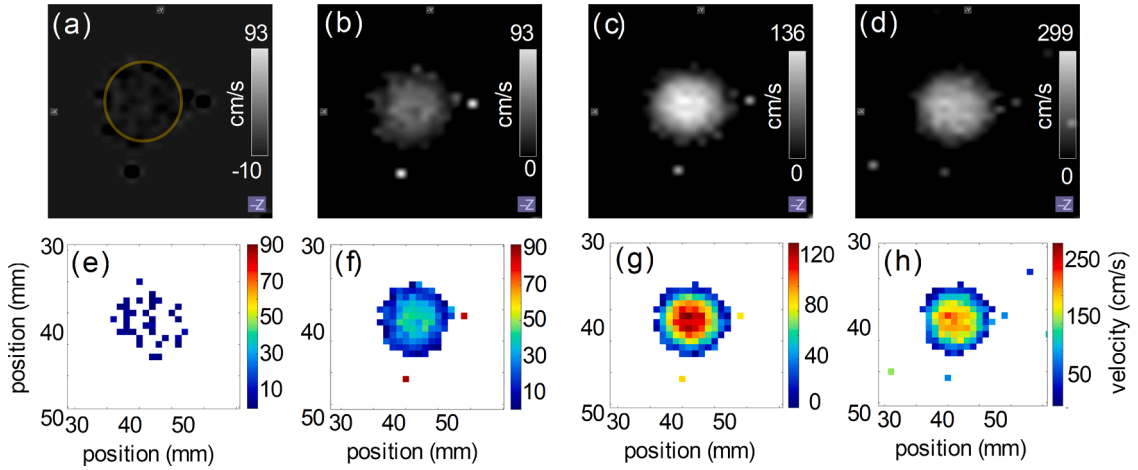

Fig. 6. MR velocity maps of ethane for different flow rates: pump off (a, e), 7.2 L/h (b, f), (c) 35.8 L/h (c, g), 71.6 L/h (d, h). For each flow setting, the maps are shown in grey scale (top) and color (bottom) to emphasize the flow profile. Note the parabolic flow profile in the colored images (f - g). The signal intensity in the phase image was lower for the highest flow (71.6 L/h, (d)) compared to the intermediate flow (35.8 L/h, (c)). The reason for this is that of the encoded velocity range was different, venc (71.6 L/h) = 300 cm/s, venc (25 L/h) = 175 cm/s. All the venc parameters for each flow are listed in Table 5. Orange circle in (a) depicts roughly the area where mean velocity values were measured and flow was calculated (Eq (16)). That final areas used for flow calculation slightly varied depending on the pixels' brightness (Table 4). Bright spots outside the gas tube in (b)-(c) are imaging artefacts.

relaxation properties of hydrocarbon gases published for different magnetic fields, we hamper finding any trend. For instance, for ethane T_1 of 1.25 s was measured at 0.63 T and 3.5 bar [34], which is similar to the value reported here (0.8 s at 7 T and 4 bar); for methane, more data can be found: $T_1 \approx 1$ s at 0.68 T and 21 bar [36], $T_1 \approx 1.1$ s at 1.43T and 70 bar [21], and $T_1 = 1.62$ s at 2.15 T and 67 bar [37]. We note that for better comparison of gas-phase relaxation data, multiple factors should be considered, i.e. gas pressure, purity of the gas or presence of paramagnetic oxygen, homogeneity of the r.f. coil providing a uniform signal excitation along the gas cell (or NMR tube).

Despite the consistency of our results, correlating with the other works, we will discuss the limitations of our gas-phase relaxometry experiments, which may explain the T_2 exceeding the T_1 values for some pressures. One can check if the diffusion of fast-moving gas molecules affects the T_2 estimation. In our CPMG sequence, a very short TE = 600 μs was employed. When the magnetic field is homogeneous enough (hence T_2^* is almost equal to T_2), such that no significant dephasing occurred for each molecule due to motion in-between refocusing 180°-pulses, then the observed decay time in the CPMG experiment is a good estimate of T_2. In our case, despite the fine tuning of shimming performed on the gas sample, the field inhomogeneities could not be eliminated entirely, which also appeared as a nonuniformly broadened spectral line (Fig. 2(a)). As a result, we obtained very short T_2^* ranging from 15 ms to 18 ms in the measured pressure range of 1.5–6 bar. In literature, the T_2^* was rarely reported with T_2 for hydrocarbon gases. For instance, Prado et al. [18] also showed a short T_2^* relaxation time of methane (1.6 ms), but that was an order of magnitude lower than the spin-spin relaxation time T_2 (13.5 ms) as measured in a glass container at 2.4 T presumably at ambient pressure (though the exact pressure for methane was unidentified by the authors).

In the case of the inhomogeneous magnetic field, the T_2^* relaxation rate can be estimated as:

$$R_2^* = R_2 + 2\pi \cdot \Delta G \cdot L \tag{18}$$

where $R_2^* = 1/T_2^*$, $R_2 = 1/T_2$, L – is the whole length of the flask (L = 80 mm), ΔG – is the gradient of magnetic field inhomogeneity. Then, using the data from Table 1, we define ΔG for our two extreme cases, i.e. pressure 1.5 bar and 6 bar: ΔG = 0.75 Hz/mm (for 1.5 bar) and ΔG = 0.80 Hz/mm (for 6 bar). Finally, the phase, φ, accumulated by spins during one TE (in our case TE = 2·τ = 600 μs) interval in the CPMG experiment can be estimated as:

$$\varphi = 2 \cdot \pi \cdot \Delta G \cdot \Delta r \cdot TE \tag{19}$$

Here, Δr is the molecule displacement calculated from Eq. (5) and using the diffusion coefficient of ethane of 0.1078 cm^2/s [38]. Thus, our dephasing was: $\varphi = 2\pi \cdot (9.0 \cdot 10^{-5})$ for 1.5 bar and $\varphi = 2\pi \cdot (9.6 \cdot 10^{-5})$ for 6

bar in radians, which is almost negligible. Overall, we suggest that our measurement of spin-spin relaxation time was accurate regarding independence from gas diffusion.

Two factors affecting the accuracy of our relaxation times measurement could be excluded: the inhomogeneity of the r.f. coil and diffusion effects. We also do not expect the presence of oxygen due to the flask's periodic flushing before the gas's measurement at each pressure. Nevertheless, the magnetic field inhomogeneity was strong, and as we mentioned in Section 3.1, the shimming could be improved by using a solvent together with the gas. Overall, we do not suggest that T_2 can be longer than T_1 for ethane and attribute the slight increase of the T_2 relaxation time over T_1 (Table 1) to the measurement error and suggest that the relaxation times are similar.

Knowing the relaxation times allowed for rapid optimization of signal intensities for FLASH 2D and 3D and RARE 2D images. Given a restricted time limit for 2D imaging of 100 s, an impressive SNR in the range of 164–430 was achieved for both sequences for a voxel of 65.7 mm^3. Typically, RARE showed higher SNR than FLASH. We consider here the poor B_0 homogeneity as one of the leading contributors: RARE depends on T_2 while FLASH depends on T_2*, which was 25–100 times different. According to the calculation, the rising of pressure led to higher spin densities and higher SNR – as observed in RARE imaging experiments (Fig. 4(b)). Concerning the FLASH experiment, the SNR followed the trend of the calculated values, including the "plateau" at 4 bar. Then, experimental SNR unexpectedly dropped at 5 bar and went back to the plateau level at 6 bar (Fig. 4(a)). Adding a 3D printed structure to the flask in the 3D FLASH acquisition did not degrade the SNR. Although the resolution (0.521 × 0.521 mm) was not sufficient enough to see fine details of the bcc structure, dim contrast from the gas penetrating in the free spaces between the spheres (~ 1 mm size) could be observed (especially in Fig. 5(d)). Not monotonous behaviour of FLASH's SNR achieved in the experiment, we attribute to the inhomogeneous field distribution of the r.f. coil (Supplementary material, Fig. S1). Thus, the "real" excitation angle, especially outside of the homogeneous coil area, could be different from the nominal Ernst angle set from the calculated T_1 relaxation time.

Using a commercial FLOWMAP sequence initially developed for studying blood flow in rodents, we measured the gas flow of a moderate-pressure range of ethane in a long tube. The encoding duration in our sequence was 0.824 ms; thus, the distance that ethane molecules can travel within one encoding step was between 0.022 cm and 0.122 cm depending on the velocity, which lies within the homogeneous length of our coil (36.6 mm) and considering the used slice thickness (40 mm). The best accuracy was achieved for the flow range between 7.2 L/h and 28.7 L/h corresponding to the velocities between 27 cm/s and 71 cm/s. Higher flow rates were underestimated (Table 4). Here we note that pressure was approximately 0.25 bar higher than the nominal value (2 bar) as measured by an additional pressure gauge on the outlet side of the tube. This could lead to slowing of the actual flow along the long tube (~ 10 m) and considering that the gas was passing through the inlet and outlet of the pump being twice smaller (~ 2 mm) than the main tube (4 mm). Thus, a solution for measuring the flow in the proximity of the MRI acquisition area should be found for future measurements. In previous publications on the velocimetry of hydrocarbon gases, velocities in a similar range, e.g. 60–93 cm/s [8,9,25] as ours, were measured by pulsed field gradient methods, though measuring accuracy was not discussed. The Reynolds numbers estimated for our experiments are all within the laminar flow regime (312 to 1699). Indeed, a characteristic slowing down of the gas flow near the inner walls of the tube, as typical for laminar flow, can be seen in the colour-coded velocity maps (Fig. 6 (f)-(h)). It was shown that hyperpolarized xenon was also employed for flow studies [13] also with the spatial resolution of (0.1 mm)^3 [39]. While xenon is sensitive to its environment, using thermally polarized gases, like hydrocarbons, can be advantageous for studying packed beds, especially in large-scale systems where high resolution is not the primary concern. Mirdrikvand et al. measured methane flowing through a 3D monolith printed from PLA material and compared the data to CFD simulations with the voxel size of (0.8 mm)^3 [40]. There, slower velocities of 17–21 cm/s were employed with the velocity encoding parameter of 30 cm/s – one order of magnitude lower than used in the current work. As a next step, after probing the gas phase imaging and velocity measurements, we aim to fully access the velocity fields of the hydrocarbon gas under various flows inside packed beds.

5. Conclusions

In conclusion, we accessed the MR imaging and flow measurements of thermally polarized ethane gas. The ^{1}H NMR spectra and relaxation properties of ethane were characterized at different pressures, revealing pressure-dependent increases in T_1 and T_2 relaxation times. The SNR of ethane images obtained using different MRI sequences was evaluated, highlighting the advantages of the RARE sequence over the FLASH imaging sequence. Moreover, RARE imaging is preferable when the uniformity of the static and RF magnetic fields is questioned. 3D MRI imaging of ethane-filled flasks demonstrated the sensitivity of MRI for imaging reaction chambers. Magnetic resonance velocimetry of ethane was performed using a velocity-encoded 2D MR sequence, showing good agreement with pump settings, especially in the slow flow range. These findings suggest that MRI can be a valuable tool for studying thermally polarized hydrocarbon gases, offering insights into their behaviour and flow dynamics in various applications. Future studies can further explore MRI techniques and optimization strategies to enhance imaging and flow measurement capabilities, including the packed bed studies for a wider range of hydrocarbon gases.

Declaration of Competing Interest

The authors declare that they have no known competing financial interests or personal relationships that could have appeared to influence the work reported in this paper.

Data availability

Data will be made available on request.

Acknowledgements

We acknowledge funding from Sonderforschungsbereich/Transregio 287 BULK-REACTION (Projekt-ID 422037413) of the Deutschen Forschungsgemeinschaft (DFG), German Federal Ministry of Education and Research (BMBF) within the framework of the e:Med research and funding concept (01ZX1915C), and GRK 2154. The authors are also grateful for the financial support by the Bruhn Foundation.

Supplementary materials

Supplementary material associated with this article can be found, in the online version, at doi:10.1016/j.jmro.2023.100137.

References

[1] C. Roloff, D. Stucht, O. Beuing, P. Berg, Comparison of intracranial aneurysm flow quantification techniques: standard PIV vs stereoscopic PIV vs tomographic PIV vs phase-contrast MRI vs CFD, J. NeuroIntervent. Surg. 11 (2019) 275–282, https://doi.org/10.1136/neurintsurg-2018-013921.

[2] C.L. Dancey, M. Balakrishnan, P. Diplas, A.N. Papanicolaou, The spatial inhomogeneity of turbulence above a fully rough, packed bed in open channel flow, Exp. Fluids 29 (2000) 402–410, https://doi.org/10.1007/s003489900107.

[3] A.J. Sederman, M.L. Johns, A.S. Bramley, P. Alexander, L.F. Gladden, Magnetic resonance imaging of liquid flow and pore structure within packed beds, Chem. Eng. Sci. 52 (1997) 2239–2250, https://doi.org/10.1016/S0009-2509(97)00057-2.

[4] A. Sträter, A. Huber, J. Rudolph, M. Berndt, M. Rasper, E.J. Rummeny, J. Nadjiri, 4D-flow MRI: technique and applications. © Georg Thieme Verlag KG, 2018, pp. 1025–1035.
[5] M. Gaeini, R. Wind, P.A.J. Donkers, H.A. Zondag, C.C.M. Rindt, Development of a validated 2D model for flow, moisture and heat transport in a packed bed reactor using MRI experiment and a lab-scale reactor setup, Int. J. Heat Mass Transf. 113 (2017) 1116–1129, https://doi.org/10.1016/j.ijheatmasstransfer.2017.06.034.
[6] M.M. Britton, MRI of chemical reactions and processes, Prog. Nucl. Magn. Reson. Spectrosc. 101 (2017) 51–70, https://doi.org/10.1016/j.pnmrs.2017.03.001.
[7] K.V. Kovtunov, E.V. Pokochueva, O.G. Salnikov, S.F. Cousin, D. Kurzbach, B. Vuichoud, S. Jannin, E.Y. Chekmenev, B.M. Goodson, D.A. Barskiy, I.V. Koptyug, Hyperpolarized NMR spectroscopy: *d* -DNP, PHIP, and SABRE techniques, Chem. Asian J. 13 (2018) 1857–1871, https://doi.org/10.1002/asia.201800551.
[8] I.V. Koptyug, S.A. Altobelli, E. Fukushima, A.V. Matveev, R.Z. Sagdeev, Thermally polarized 1H NMR microimaging studies of liquid and gas flow in monolithic catalysts, J. Magn. Reson. 147 (2000) 36–42, https://doi.org/10.1006/jmre.2000.2186.
[9] I.V. Koptyug, L.Yu. Ilyina, A.V. Matveev, R.Z. Sagdeev, V.N. Parmon, S.A. Altobelli, Liquid and gas flow and related phenomena in monolithic catalysts studied by 1H NMR microimaging, Catal. Today 69 (2001) 385–392, https://doi.org/10.1016/S0920-5861(01)00396-0.
[10] E.V. Pokochueva, D.B. Burueva, O.G. Salnikov, I.V. Koptyug, Heterogeneous catalysis and parahydrogen-induced polarization, ChemPhysChem 22 (2021) 1421–1440, https://doi.org/10.1002/cphc.202100153.
[11] D.A. Barskiy, K.V. Kovtunov, E.Y. Gerasimov, M.A. Phipps, O.G. Salnikov, A. M. Coffey, L.M. Kovtunova, I.P. Prosvirin, V.I. Bukhtiyarov, I.V. Koptyug, E. Y. Chekmenev, 2D mapping of NMR signal enhancement and relaxation for heterogeneously hyperpolarized propane gas, J. Phys. Chem. C. 121 (2017) 10038–10046, https://doi.org/10.1021/acs.jpcc.7b02506.
[12] E. Brunner, M. Haake, L. Kaiser, A. Pines, J.A. Reimer, Gas flow MRI using circulating laser-polarized129xe, J. Magn. Reson. 138 (1999) 155–159, https://doi.org/10.1006/jmre.1998.1675.
[13] S.-I. Han, K.L. Pierce, A. Pines, NMR velocity mapping of gas flow around solid objects, Phys. Rev. E. 74 (2006), 016302, https://doi.org/10.1103/PhysRevE.74.016302.
[14] G. Pavlovskaya, J. Six, T. Meersman, N. Gopinathan, S.P. Rigby, NMR imaging of low pressure, gas-phase transport in packed beds using hyperpolarized xenon-129, AIChE J. 61 (2015) 4013–4019, https://doi.org/10.1002/aic.14929.
[15] C.M. Boyce, N.P. Rice, A. Ozel, J.F. Davidson, A.J. Sederman, L.F. Gladden, S. Sundaresan, J.S. Dennis, D.J. Holland, Magnetic resonance characterization of coupled gas and particle dynamics in a bubbling fluidized bed, Phys. Rev. Fluids 1 (2016), 074201, https://doi.org/10.1103/PhysRevFluids.1.074201.
[16] D.J. Holland, D.M. Malioutov, A. Blake, A.J. Sederman, L.F. Gladden, Reducing data acquisition times in phase-encoded velocity imaging using compressed sensing, J. Magn. Reson. 203 (2010) 236–246, https://doi.org/10.1016/j.jmr.2010.01.001.
[17] S.V. Elgersma, A.J. Sederman, M.D. Mantle, C.M. Guédon, G.J. Wells, L.F. Gladden, Magnetic resonance velocity imaging of turbulent gas flow in a packed bed of catalyst support pellets, Chem. Eng. J. (2023), 145445, https://doi.org/10.1016/j.cej.2023.145445.
[18] P.J. Prado, B.J. Balcom, I.V. Mastikhin, A.R. Cross, R.L. Armstrong, A. Logan, Magnetic Resonance Imaging of Gases: a Single-Point Ramped Imaging withT1Enhancement (SPRITE) Study, J. Magn. Reson. 137 (1999) 324–332, https://doi.org/10.1006/jmre.1998.1674.
[19] K.V. Kovtunov, A.S. Romanov, O.G. Salnikov, D.A. Barskiy, E.Y. Chekmenev, I. V. Koptyug, Gas phase UTE MRI of propane and propene, Tomography 2 (2016) 49–55, https://doi.org/10.18383/j.tom.2016.00112.
[20] J. Ulpts, W. Dreher, M. Klink, J. Thöming, NMR imaging of gas phase hydrogenation in a packed bed flow reactor, Appl. Catal. A 502 (2015) 340–349, https://doi.org/10.1016/j.apcata.2015.06.011.
[21] A. Duchowny, P.M. Dupuy, H.C. Widerøe, O.J. Berg, A. Faanes, A. Paulsen, H. Thern, O. Mohnke, M. Küppers, B. Blümich, A. Adams, Versatile high-pressure gas apparatus for benchtop NMR: design and selected applications, J. Magn. Reson. 329 (2021), 107025, https://doi.org/10.1016/j.jmr.2021.107025.
[22] F. Aiello, J. Gerretzen, M.G. Simons, A.N. Davies, P. Dani, A multivariate approach to investigate the NMR CPMG pulse sequence for analysing low MW species in polymers, Magn. Reson. Chem. 59 (2021) 172–186, https://doi.org/10.1002/mrc.5100.
[23] H.Y. Carr, E.M. Purcell, Effects of diffusion on free precession in nuclear magnetic resonance experiments, Phys. Rev. 94 (1954) 630–638, https://doi.org/10.1103/PhysRev.94.630.
[24] S. Meiboom, D. Gill, Modified spin-echo method for measuring nuclear relaxation times, Rev. Sci. Instrum. 29 (1958) 688–691, https://doi.org/10.1063/1.1716296.
[25] I.V. Koptyug, A.V. Matveev, S.A. Altobelli, NMR studies of hydrocarbon gas flow and dispersion, Appl. Magn. Reson. 22 (2002) 187, https://doi.org/10.1007/BF03166102.
[26] R.E. Hendrick, J.B. Kneeland, D.D. Stark, Maximizing signal-to-noise and contrast-to-noise ratios in flash imaging, Magn. Reson. Imaging 5 (1987) 117–127, https://doi.org/10.1016/0730-725X(87)90041-5.
[27] R.E. Hendrick, Sampling time effects on signal-to-noise and contrast-to-noise ratios in spin-echo MRI, Magn. Reson. Imaging 5 (1987) 31–37, https://doi.org/10.1016/0730-725X(87)90481-4.
[28] R.W. Brown, Y.-C.N. Cheng, E.M. Haacke, M.R. Thompson, R. Venkatesan, Magnetic Resonance imaging: Physical Principles and Sequence Design, 2nd ed., John Wiley & Sons, Inc, Hoboken, New Jersey, 2014.
[29] B. Gruber, M. Froeling, T. Leiner, D.W.J. Klomp, RF coils: a practical guide for nonphysicists: RF Coils, J. Magn. Reson. Imaging. 48 (2018) 590–604, https://doi.org/10.1002/jmri.26187.
[30] M.H. Levitt, Spin Dynamics: Basics of Nuclear Magnetic Resonance, John Wiley & Sons, 2013.
[31] P.M. Singer, D. Asthagiri, W.G. Chapman, G.J. Hirasaki, NMR spin-rotation relaxation and diffusion of methane, J. Chem. Phys. 148 (2018), 204504, https://doi.org/10.1063/1.5027097.
[32] Y. Zhang, G.J. Hirasaki, W.V. House, R. Kobayashi, Oil and Gas NMR Properties: The Light And Heavy Ends, 2002. SPWLA-2002-HHH.
[33] J.A. Zega, W.V. House, R. Kobayashi, A corresponding-states correlation of spin relaxation in normal alkanes, Physica A 156 (1989) 277–293, https://doi.org/10.1016/0378-4371(89)90123-4.
[34] J.D. King, W.L. Rollwitz, C.I. Nicholls, A.D. Los Santos, Hydrocarbon Gas Measurements Using Nuclear Magnetic Resonance, 1992, 5,122,746.
[35] M. Bloom, F. Bridges, W.N. Hardy, Nulcear spin relaxation in gaseous methane and its deuterated modifications, Can. J. Phys. 45 (1967) 3533–3554, https://doi.org/10.1139/p67-299.
[36] C.J. Gerritsma, P.H. Oosting, N.J. Trappeniers, Proton-spin-lattice relaxation and self-diffusion in methanes, Physica 51 (1971) 381–394, https://doi.org/10.1016/0031-8914(71)90048-6.
[37] S.-W. Lo, Correlations of NMR Relaxation Time with Viscosity/Temperature, Diffusion Coefficient and Gas/Oil Ratio of Methane-Hydrocarbon Mixtures, Rice University, 2000.
[38] A. Boushehri, J. Bzowski, J. Kestin, E.A. Mason, Equilibrium and transport properties of eleven polyatomic gases at low density, J. Phys. Chem. Ref. Data 16 (1987) 445–466, https://doi.org/10.1063/1.555800.
[39] L.G. Kaiser, T. Meersmann, J.W. Logan, A. Pines, Visualization of gas flow and diffusion in porous media, Proc. Natl. Acad. Sci. U.S.A. 97 (2000) 2414–2418, https://doi.org/10.1073/pnas.050012497.
[40] M. Mirdrikvand, M. Sadeghi, G.R. Pesch, W. Dreher, J. Thöming, Full-field comparison of MRV and CFD of gas flow through regular catalytic monolithic structures, Processes 9 (2021) 566, https://doi.org/10.3390/pr9030566.